

Ge/BaF₂ thin-films for surface micromachined mid-wave and long-wave infrared reflectors

Gurpreet S. Gill^{a,*}, Dhirendra K. Tripathi,^a Adrian Keating,^b
Gino Putrino,^a Konkaduwa Kamala Mesthrige Buddhika Dilusha Silva,^a
Mariusz Martyniuk,^{a,c} and Lorenzo Faraone^{a,c}

^aThe University of Western Australia, School of Engineering, Department of Electrical, Electronic and Computer Engineering, Perth, Western Australia, Australia

^bThe University of Western Australia, School of Engineering, Department of Mechanical Engineering, Perth, Western Australia, Australia

^cThe University of Western Australia, ARC Centre of Excellence for Transformative Meta-Optical Systems, Perth, Western Australia, Australia

Abstract. High performance distributed Bragg reflectors (DBRs) are key elements to achieving high finesse MEMS-based Fabry–Pérot interferometers (FPIs). Suitable mechanical parameters combined with high contrast between the refractive indices of the constituent optical materials are the main requirements. In this paper, Germanium (Ge) and barium fluoride (BaF₂) optical thin-films have been investigated for mid-wave infrared (MWIR) and long-wave infrared (LWIR) filter applications. Thin-film deposition and fabrication processes were optimised to achieve mechanical and optical properties that provide flat suspended structures with uniform thickness and maximum reflectivity. Ge-BaF₂-Ge 3-layer solid-material DBRs have been fabricated that matched the predicted simulation performance, although a degradation in performance was observed for wavelengths beyond 10 μm that is associated with optical absorption in the BaF₂ material. Ge-Air-Ge 3-layer air-gap DBRs, in which air rather than BaF₂ served as the low refractive index layer, were realized to exhibit layer flatness at the level of 10 to 20 nm across lateral DBR dimensions of several hundred micrometers. Measured DBR reflectance was found to be $\geq 90\%$ over the entire wavelength range of the MWIR band and for the LWIR band up to a wavelength of 11 μm . Simulations based on the measured DBR reflectance indicates that MEMS-based FPIs are able to achieve a peak transmission of $\geq 90\%$ over the entire MWIR band and up to 10 μm in the LWIR band, with a corresponding spectral passband of ≤ 50 nm in the MWIR and < 80 nm in the LWIR. © The Authors. Published by SPIE under a Creative Commons Attribution 4.0 International License. Distribution or reproduction of this work in whole or in part requires full attribution of the original publication, including its DOI. [DOI: [10.1117/1.JOM.2.1.011002](https://doi.org/10.1117/1.JOM.2.1.011002)]

Keywords: optical thin-films; distributed Bragg reflector; Fabry–Pérot interferometers; long-wave infrared; mid-wave infrared.

Paper 21012SS received Jun. 24, 2021; accepted for publication Oct. 8, 2021; published online Jan. 4, 2022.

1 Introduction

Spectrometers^{1–7} in the mid-wave infrared (MWIR: 3 to 5 μm) and long-wave infrared (LWIR: 8 to 12 μm) wavelength ranges are of interest for infrared (IR) spectroscopy,^{8–11} multi/hyper-spectral imaging,^{12–16} and compositional analysis^{11,17} due to their inherent ability to identify the unique absorption and/or reflected spectra of elements and compounds. Multi/hyper-spectral imaging is commonly differentiated based on the number of spectral channels, where hyperspectral imaging systems generally collect more than 100 adjoining spectral bands and multispectral imaging systems typically acquire < 20 non-adjoining spectral bands,^{12,16,18,19} even though there is no agreement on precise values.

*Address all correspondence to Gurpreet S. Gill, gurpreet.gill@research.uwa.edu.au

Fabry–Pérot interferometers (FPIs) provide a spectrometer architecture that is compatible with thin-film surface-micromachined microelectromechanical systems (MEMS). FPIs consist of two mirrors, which in a MEMS implementation generally consist of a pair of distributed Bragg reflectors (DBRs), separated by an optical cavity. The thicknesses of the constituting DBR layers and the separation between the DBRs are selected based on the spectral band of operation.^{20,21} Conventional spectrometers use bulky and fragile optics, which makes them non-portable and hinders their suitability for in-field deployment. However, FPIs fabricated using MEMS technology have a small footprint, are mechanically robust, use very little power, and are hence field-portable. This ability to overcome many of the drawbacks of conventional spectrometers systems^{3,20,21} makes them attractive for deployment in platforms requiring low size, weight, and power (SWaP), such as unmanned autonomous vehicles (UAVs), drones, satellites, and mobile phones.

Typically, MEMS-based filters are either implemented using a guided-mode resonance effect or a multiple-beam interference-effect. A study on the guided-mode resonance for the realization of resonant filters has been well presented by the group of Magnusson,^{22–24} and Ko et al.²⁴ have recently published a study claiming realization of prototypes. In the latter work, the fabricated devices had a very large die size (width: 26 mm, height: 18 mm) and tuning of the transmission peak was performed mechanically, by an external tuning mechanism resulting in a relatively bulky system. Nevertheless, as a demonstration technology, this approach is useful for benchtop implementations, which do not demand low SWaP or integration on portable platforms.

On the other hand, in a multiple-beam interference approach, multiple beams are captured in a cavity between two mirror plates or DBRs to realize FPIs. In MEMS implementations, DBRs for the FPIs can be fabricated by depositing an alternating sequence of low-absorbing dielectric layers of high- and low-refractive index materials.²⁵ In this configuration, $\lambda/4$ -thick optical films are deposited, where the thickness of each optical layer is equivalent to one quarter of the wavelength for which the DBR is designed.^{12,26,27} High reflectivity of the DBRs is assured if there is a high contrast between the refractive indices of the high- and low index materials, which provides a pathway toward the realization of narrowband FPIs. In this paper, germanium (Ge) and barium fluoride (BaF₂)/air have been considered as the high and low refractive index materials/media, respectively, for the fabrication of DBRs. The $\lambda/4$ -thickness²⁸ and optical constants^{29–32} for the thin-films required for applications in the technologically important MWIR and LWIR bands are listed in Table 1. Ge thin-films have been previously explored by several research groups^{2,12,21,27,33–36} to fabricate DBRs in the IR region. In particular, our group at The University of Western Australia^{12,21,27,33,34} and InfraTec GmbH^{2,36} have used Ge thin-films as

Table 1 Material parameters for the design of MWIR and LWIR DBRs at center wavelengths of 4 and 10 μm , respectively. This table shows the calculated $\lambda/4$ -thicknesses for materials, targeted and achieved mirror flatness, and simulated and measured mirror reflectance. Note that the deposited layer thicknesses are within a tolerance of $\pm 5\%$.

Wavelength range	CW ^a [μm]	Material	$\lambda/4$ thickness [nm]	Refractive index at 10 μm [Ref.]	DBR type	DBR flatness [nm]		DBR reflectance [%]			
						Targeted	Achieved	Simulated		Measured	
								OEWB ^a	PR ^a	OEWB ^a	PR ^a
MWIR (3 to 5 μm)	4	Ge	250	3.95 ^{29,30}	α_{MW}	15 to 25 < $\lambda/200$	10 to 20	>95	98.5	>90	97.2
		BaF ₂	720	1.4 ^{31,32}							
		Air	1000	1	β_{MW}					>97	99
LWIR (8 to 12 μm)	10	Ge	625	3.95 ^{29,30}	α_{LW} (8 to 10 μm)	40 to 60 < $\lambda/200$	10 to 20	>96	98.5	>96.5	97.5
		BaF ₂	1800	1.4 ^{31,32}							
		Air	2500	1	β_{LW}					>97	99

^aCW – center wavelength, OEWB – Over entire wavelength band, PR – Peak reflectance.

a high refractive index material along with low refractive index materials such as SiO_x, SiN_x, and ZnS for the fabrication of shortwave and longwave IR FPIs. The studies based on SiO_x and SiN_x are mainly focused in the short wave infrared region since SiO_x and SiN_x are absorbing in the LWIR spectral band, which renders them unsuitable for the development of narrowband FPIs at LWIR wavelengths. On the other hand, ZnS is non-absorbing in the LWIR region but its refractive index of 2.2 as a low refractive index material combined with Ge is not sufficient to provide a high refractive index contrast (a key component to developing narrowband FPIs). Thus, it is impractical for ZnS-based FPIs to achieve a narrow linewidth (typically $\leq 1\%$ of the design wavelength as inferred from the following studies^{7,12,16,37-39}) in the LWIR region for hyperspectral sensing and imaging, although these FPIs would be suitable for multi-spectral sensing and imaging. To fill this gap, we propose BaF₂ as a low refractive index material due to its low refractive index in the LWIR spectral band,^{31,32} combined with Ge for the development of narrow-linewidth FPIs in the LWIR spectral band for hyperspectral sensing and imaging applications. Within the MWIR and LWIR spectral bands, the availability of materials with adequate optical and mechanical properties is limited, especially in the LWIR. While BaF₂ thin-films have previously been used for optical coatings,^{40,41} the applicability and compatibility of the material with micromachining processes to enable high performance wavelength discrimination in the MWIR and LWIR band has not previously been studied. Although BaF₂ is a highly attractive optical material due to its low refractive index^{31,32} in the MWIR and LWIR wavelength ranges and can significantly boost the optical performance of optical MEMS devices, it is not yet a mature technology for micromachining applications from the application point of view. For example, BaF₂ is slightly hygroscopic⁴² in nature, and therefore requires process development for adopting it in MEMS fabrication processes, where water is the most commonly used solvent for cleaning the samples. Furthermore, significant challenges associated with the thermal deposition of films that are several micrometers thick must be resolved since such layers are required to achieve the $\lambda/4$ -wavelength thickness requirement for filter applications in the LWIR region. Finally, the process compatibility of multilayer Ge/BaF₂ thick films must be addressed to demonstrate the feasibility of this material combination to enhance the available choices when designing filters for MWIR and LWIR applications.

The use of Ge/BaF₂ stacks in these applications introduce challenges in controlling residual stresses and surface roughness while maintaining the high optical performance expected from BaF₂ layers. Adhesion of these materials between themselves and other commonly used MEMS materials throughout the range of wet and dry etching steps is required during the fabrication of complex MEMS-based structures and must be addressed. In this work, we have thoroughly addressed these challenges, in order to take advantage of the exceptional optical properties of BaF₂ thin-films for optical MEMS applications. For optimal performance, a high level of parallelism between the DBRs is required, typically better than $\lambda/10$ or $\lambda/20$ for MEMS-based optical applications.⁴³⁻⁴⁶ Our efforts in this work culminate in fabricating layers with mirror parallelism exceeding a level of $\lambda/200$ for the suspended mirror layers. This work provides reliable and reproducible methods to develop high performing surface micromachined DBRs for the MWIR and LWIR wavelength regions using thermally evaporated BaF₂ as a low refractive index material and their suitability in the development of MEMS-based optical FPIs. Throughout this work, Ge thin-films have been used as the high refractive index material and two alternatives for the low refractive index layers have been explored, as schematically shown in Fig. 1(a). We have investigated the use of either BaF₂ thin-films or an air-gap as the low-refractive index media for the DBRs. Figure 1(b) shows the 3D representation of an air-gap DBR. To improve visualization, the top Ge layer is rendered to show the profile of the underlying sacrificial layer. Thin-film deposition conditions have been optimized to yield thin-film layers having low stress, low surface roughness, and excellent optical properties in order to demonstrate solid-material DBRs as well as suspended Ge air-gap DBRs with $200\ \mu\text{m} \times 200\ \mu\text{m}$, $500\ \mu\text{m} \times 500\ \mu\text{m}$, and $1\ \text{mm} \times 1\ \text{mm}$ optical areas toward their subsequent incorporation into FPIs that can be hybridized with either single point IR detectors or focal plane imaging arrays. Lastly, this paper predicts the expected characteristics of FPIs based on the reflectance response of the fabricated DBRs via optical simulations. The fabrication of experimental FPIs is beyond the scope of this paper and will be addressed in future studies.

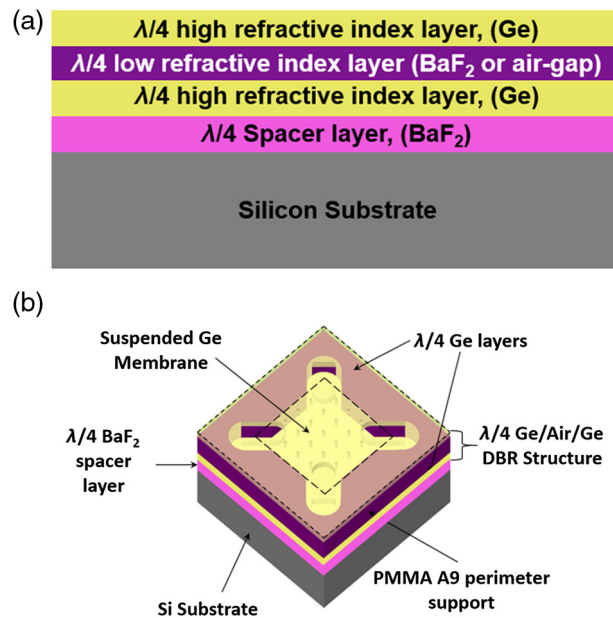


Fig. 1 (a) Cross-section of quarter wavelength thick layers of a DBR utilising Ge as the high refractive index layer and either BaF₂ or air-gap as the low refractive index medium. (b) 3D representation of the air gap DBRs, the top Ge layer is colourised to show the profile of the underlying sacrificial layer for visualisation purposes.

2 Experimental Details and DBR Fabrication Process

2.1 Thin-Film Deposition

The Ge and BaF₂ layers were deposited under high vacuum ($<10^{-6}$ mbar), using a thermal evaporator, with an in-situ thermocouple to monitor the substrate temperature. In order to investigate the impact of substrate temperature on the residual stress of Ge and BaF₂ thin-films, the depositions were initiated at four different substrate temperatures: 25°C, 50°C, 100°C, and 150°C using a substrate heating block. Since a cooling system was not integrated into our system, a rise in substrate temperature was observed during the deposition due to radiative heating from the evaporation source for depositions initiated at temperatures 50°C and below. Therefore, for depositions initiated at temperatures 25°C and 50°C, the substrate temperature was kept within the temperature windows of 25°C to 70°C and 50°C to 70°C, respectively. For depositions initiated at temperatures $\geq 100^\circ\text{C}$, the temperature variation could readily be controlled within a tolerance of $\pm 5^\circ\text{C}$. It is noted that the thin-films were deposited without breaking vacuum either in a single run or by adopting a multi-step deposition technique. Substrate heating was available both before and during the deposition to control the substrate temperature. On completion of the deposition run, the substrate was allowed to cool down to room temperature before opening the chamber.

The deposition of Ge thin-films was performed at a deposition rate of $1.5 \pm 0.1 \text{ \AA/s}$ in a single continuous run satisfying the above-mentioned conditions. Figure 2 shows exemplar temperature profiles for Ge thin-films deposited at 50°C (green) and 100°C (blue). The dashed lines in Fig. 2 represent the substrate heating and cooling periods before and after the thin-film deposition periods represented by the solid lines. However, deposition of BaF₂ thin-films was performed at a deposition rate of $5 \pm 0.2 \text{ \AA/s}$, and a multi-step deposition technique was adopted for depositions initiated at temperatures 25°C and 50°C to achieve the desired thicknesses mentioned in Table 1. Once the substrate temperature reached the maximum limit of the temperature window, the deposition was stopped to allow the temperature to drop to the minimum limit of the temperature window without breaking vacuum. Consequently, the deposition of BaF₂ thin-films

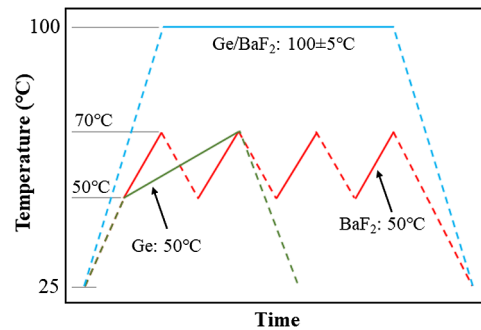


Fig. 2 Substrate temperature profiles for Ge and BaF₂ thin-films deposited at 50°C and 100°C. The dashed lines represent the substrate heating and cooling periods before and after the thin-film deposition periods represented by the solid lines.

was divided into two and four steps of equally distributed thicknesses for MWIR and LWIR DBRs, respectively. Although a multi-step deposition technique was not required for depositions initiated at 100°C and 150°C, to ensure sample-to-sample consistency, the depositions initiated at these temperatures were also performed in steps and provide the same waiting period between each deposition step for the BaF₂ thin-films. An exemplar of temperature profiles for BaF₂ thin-films deposited at 50°C (red) and 100°C (blue) is shown in Fig. 2.

A significant challenge during the deposition of the relatively thick Ge and BaF₂ thin-films of the order of 1 μm in thickness was the integrity of the evaporation sources and materials for such a prolonged time and the sudden failure of the quartz crystal microbalance^{47,48} during deposition due to overheating. Therefore, it becomes critically important to select an evaporation source that is compatible with the deposited material and can survive the long deposition time. In the case of Ge, the issue of boat failure was quite common in the middle of a deposition. Therefore, the deposition of Ge thin-films was performed using two boats in one run by switching between boats. On the other hand, a multi-chamber baffled boxes chimney boat was used to deposit the comparatively thick BaF₂ layers and to prevent any spitting or streaming. The issue of boat failure was not observed during the deposition of BaF₂ films. However, a sudden failure of the quartz crystal microbalance was observed regularly during BaF₂ deposition in a single run due to excessive radiative heat from the evaporation source. The adopted multi-step deposition technique helps to prevent the sudden failure of the quartz crystal microbalance and also provides reasonable control of the thin-film surface roughness.

2.2 DBR Fabrication Process

This section presents the fabrication process of DBRs for the MWIR and LWIR wavelength spectral bands. For a better understanding of the fabrication process, the solid-material and air-gap DBRs are categorised as α - and β - series, respectively. The α - series DBRs consisted of $\lambda/4$ -thick Ge/BaF₂/Ge layers deposited on an Si substrate coated with a $\lambda/4$ -thick BaF₂ spacer layer, whereas the, β - series DBRs consisted of $\lambda/4$ -thick Ge/Air/Ge layers. The intermediate BaF₂ mirror layer existing in α - series DBRs was replaced with an air-gap in β - series DBRs using surface micromachining techniques. The subscripts MW and LW will be used to represent the mid-wave and long-wave IR bands, respectively. The performance of DBRs, especially those with an internal air-gap (β - series DBRs), will depend on the substrate and on the residual stress of thin-film layers on that substrate since compressive residual stress of thin-films can lead to various deformations such as tilt, bending, and buckling. Through an appropriate control of material residual stress, the degree of tilt and bending in any suspended layers can be minimized to yield good optical quality in the fabricated DBRs. A process flow for the fabrication of α - and β - series DBRs is shown in Fig. 3.

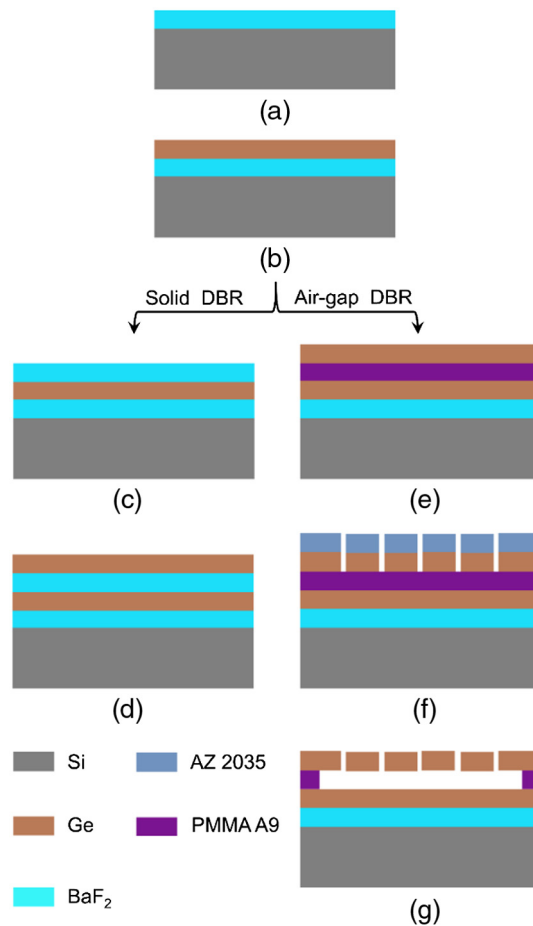


Fig. 3 The DBR fabrication process. Thicknesses are not to scale. (a) Deposition of a $\lambda/4$ -thick low refractive index BaF₂ spacer layer on Si substrate; (b) deposition of first high refractive index Ge layer. In the case of α -series DBRs; (c)–(d) deposition of $\lambda/4$ -thick low and high refractive index BaF₂ and Ge layers. In the case of β -series DBRs: (e) spinning and hard-baking of PMMA A9 sacrificial layer and deposition of the second quarter-wavelength thick Ge thin film on top of PMMA A9; (f)–(g) patterning of etching holes through the top Ge layer using an AZ2035 photoresist mask, and dry release of air-gap DBRs via the removal of PMMA layer in the O₂ plasma.

2.2.1 Common steps for α - and β -DBR's

- a. A low refractive index $\lambda/4$ -thick BaF₂ spacer layer was thermally evaporated on the starting Si-substrates as shown in Fig. 3(a). This low refractive index spacer layer is used to differentiate the high-low-high refractive index 3-layer mirror from the substrate and to improve the optical performance of the mirror.
- b. As shown in Fig. 3(b), a $\lambda/4$ -thickness Ge layer was thermally evaporated onto the BaF₂ spacer layer. For the MWIR and LWIR DBRs, the targeted $\lambda/4$ -thicknesses of Ge thin-films were 250 and 625 nm, respectively.

2.2.2 α -series DBR's

- c and d. For α -series DBRs, low and high refractive index $\lambda/4$ -thickness BaF₂ and Ge layers were deposited on top of the first Ge layer as shown in Figs. 3(c) and 3(d), respectively. At this stage, the α -series DBRs were ready for optical characterization.

2.2.3 β - series DBRs

- e. For β - series DBRs, a $\lambda/4$ -thickness MicroChem Corp. PMMA A9 sacrificial layer was spun at 4000 rpm for MWIR DBRs and at 1250 rpm for LWIR DBRs to realize $\lambda/4$ -air cavities for both wavelength ranges, as shown in Fig. 3(e). The PMMA A9 sacrificial layer was soft-baked at 180°C for 2 min, and then the temperature was ramped to 210°C for a total of 15 min to cure it fully. In order to improve the adhesion of PMMA A9, adhesion promoter Brewer Science APX-K1 was spun at 4000 rpm and baked at 130°C for 30 s before spin-depositing the PMMA. The PMMA A9 sacrificial layer was followed by a thermally evaporated $\lambda/4$ -thickness Ge layer, as shown in Fig. 3(e).
- f. Subsequently, for free-standing β - series DBRs, the top Ge layer was patterned with the help of negative photoresist AZ2035 to create perforation holes (6 μm in diameter) in the top Ge layer using CF₄ based plasma etching [see Fig. 3(f)] to facilitate removal (release) of the PMMA sacrificial layer.
- g. Finally, the negative photoresist and sacrificial layer were removed at the same time in an O₂ plasma in a March PM-600 Barrel Asher for 20 min with 120 W RF power at 1 Torr chamber pressure. After the dry release of the sacrificial layer, the top Ge layer was suspended over the bottom Ge layer forming an air cavity DBR, as shown in Fig. 3(g). At this stage, the β - series DBRs were ready for optical characterization.

The above methods were used to fabricate α - series DBRs, as well as β - series DBRs with various optical areas of 200 $\mu\text{m} \times 200 \mu\text{m}$, 500 $\mu\text{m} \times 500 \mu\text{m}$, and 1 mm \times 1 mm. The measured thicknesses of deposited films were all within the targeted value tolerance of $\pm 5\%$. Where the actual measured thickness of each thin-film is mentioned in the appendix (see Fig. 12).

2.3 Measurement and Characterization Techniques

Optical characterization techniques were used to estimate the thin-film stress using a radius of curvature measurements, to extract their optical properties such as refractive index (n) and extinction coefficient (k) from the transmission spectra of thin-films, to determine the flatness of suspended membranes, and to measure optical reflection spectra. The stress of thin-films was measured by applying Stoney's formula.^{49,50} To measure the thin-film intrinsic stress, the $\lambda/4$ -thick Ge and BaF₂ films of targeted center LW of 10 μm were deposited on 100 μm thick silicon substrates. In order to estimate the residual stress of thin-films, a Zygo Newview 6 K white light optical surface profilometer was used to measure the radius of curvature of 100- μm thin Si substrates before and after deposition. The same tool was later used to perform flatness measurement over the free-standing membranes of fabricated β - series DBRs.

A Spotlight 200i FT-IR Microscopy System with Spectrum Two by Perkin Elmer was used to measure the transmission response of thin-films and DBR reflectance. Transmission measurements were performed with the FTIR Spectrum Two, and the refractive index (n) and extinction coefficient (k) of the materials were extracted from the transmission response. This study was mainly focused on the less well-known BaF₂ layers to investigate the refractive index and extinction coefficient in the IR region, which were then compared with past studies.^{31,32} Finally, the BaF₂ thin-films were incorporated as an alternating layer with Ge thin-films to realize DBRs. The reflectance measurements of the DBRs were performed using the FTIR Microscope, which allows direct measurement of the DBR reflectance. The microscope beam was focused in the center of the DBR, to a measurement spot size of approximately 35 $\mu\text{m} \times 35 \mu\text{m}$. The optical transfer matrix method (OpenFilters⁵¹) was used to simulate the reflectance of the multilayer thin-film DBR stack of the fabricated devices,^{25,52} with the experimentally determined thicknesses and optical constants of Ge and BaF₂ being used in the model.

Cross-sectional analysis of DBRs was performed using an FEI Helios Nanolab ultra high-resolution scanning electron microscope (SEM) equipped with focused ion beam (FIB) technology. The elemental mapping and compositional analysis of thin-films over a FIB-milled cross-section were enabled by energy-dispersive spectroscopy (EDS). This allowed the quality of thin-film interfaces, composition, and their elemental distribution to be determined over the thicknesses of the deposited thin-films.

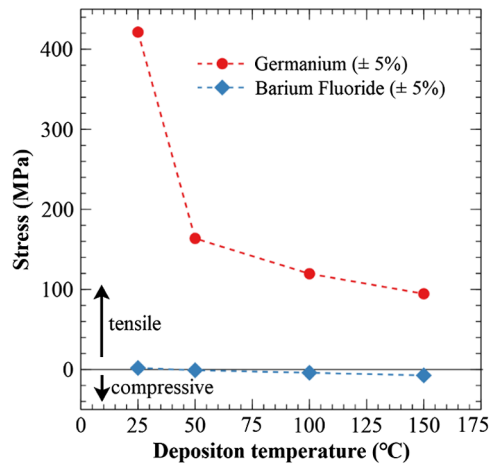


Fig. 4 Residual stress in thermally deposited Ge and BaF₂ $\lambda/4$ -thick films as a function of initial deposition temperature. Thin-film stress was calculated using Stoney's formula by measuring the thin film stress-induced substrate curvature.

3 Characterization of Fabricated Thin-Films and DBRs

3.1 Thin-Film Stress

Figure 4 shows the thin-film stress values as a function of the starting deposition temperature calculated from Stoney's formula for the deposited Ge and BaF₂ thin-films. Ge thin-films were found to be characterised by residual tensile stress, which decreased monotonically with increasing substrate temperature. The measured tensile stress for a $\lambda/4$ Ge thin-films was 421 MPa when the deposition started at room temperature. This stress value reduced significantly to 163 MPa when the deposition was initiated at a temperature of 50°C. Our experiments indicate that a manageable level of tensile thin-film stress (<100 MPa) can be achieved when the deposition was initiated and maintained at 150°C, as shown in Fig. 4. On the other hand, BaF₂ exhibits only a relatively small change in stress with deposition temperature, albeit with a change from a tensile to compressive nature, over the entire temperature range investigated (see Fig. 4).

3.2 Characterization of Optical Parameters: Refractive Index and Extinction Coefficient

Ge and BaF₂ have been used as the high and low refractive index material, respectively, in DBR fabrication because of their attractive near-zero absorption in the LWIR region as well as their high refractive index contrast.^{29-32,53} The optical properties of BaF₂ were extracted from the transmission response of a 2.6- μm thick layer of BaF₂ deposited on a silicon substrate. This was recorded for wavelengths from 1.2 to 12 μm and analysed with the Cauchy dispersion model using general-purpose software (NKDMatl⁵⁴) to extract the n - and k -values. The recorded transmission spectrum was found to adequately match the Cauchy dispersion model for wavelengths up to 5.5 μm ; however, the quality of the fit was reduced for wavelengths longer than 5.5 μm . Therefore, we used the extracted n - and k -values only for wavelengths below 5.5 μm , which are indicated in Figs. 5(a) and 5(b) as magenta open diamond symbols. For the purpose of comparison, Fig. 5(a) includes n -values obtained by Query,³² as indicated by the red solid line; whereas k -values reported were zero and are not represented on the log scale in Fig. 5(b). We have measured n -values of 1.37 for BaF₂ and k -values of near-zero, which compares favourably with the measurements of Query, where the n -values were found to range from 1.47 to 1.36 with a k -value of zero over the wavelength range 0.6 to 12.2 μm . Based on this favourable agreement between our measurement and previous literature for wavelengths below 5.5 μm , our measured n - and k -values were linearly extrapolated into the LWIR region, as indicated in Figs. 5(a) and 5(b) with magenta dashed lines. This will be discussed later in the paper with a comparison

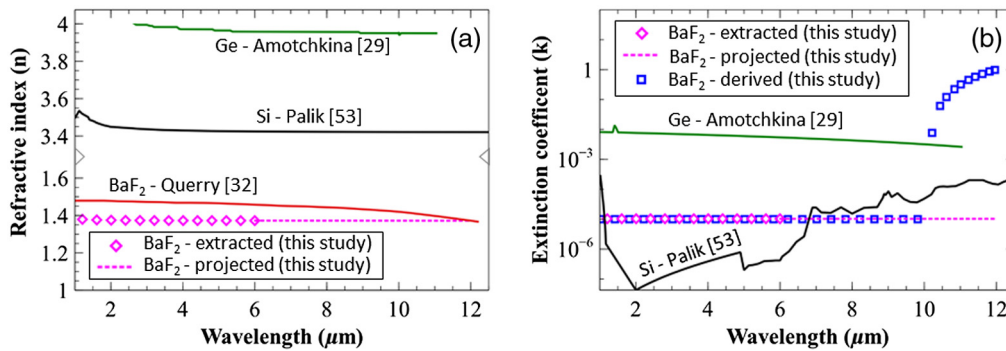


Fig. 5 Measured (a) refractive index (n), and (b) extinction coefficient (k) of BaF₂ thin-films and their comparison with previous studies. The n - and k -values in this study (indicated as “extracted”) were measured from the transmission of a 2.6- μm thick BaF₂ layer, which was fitted with the Cauchy dispersion model only for wavelengths shorter than 5.5 μm . Stimulated by a favourable agreement with prior literature (Query³²) the n - and k -values were linearly projected beyond 5.5 μm into the LWIR region for wavelengths up to 12 μm and are indicated by dashed lines. The reported k -values for BaF₂ were zero and are not represented on the log scale in (b). The BaF₂ k -values indicated as “derived” were obtained in order to achieve agreement between the measured and simulated reflectance spectra of α_{LW} by adjusting the k -values during fitting iterations. The n - and k -values of Si, Ge, and BaF₂ used in this study have been taken from Refs. 29–32, 53, and 55.

to the data derived from the characterised DBR performance, which is indicated in Fig. 5(b) as blue open square symbols. Ge and Si n - and k -values used in this study are also shown in Fig. 5.^{29,53,55}

3.3 Structural Characterization of DBRs

Extensive characterization was performed to investigate the layered structures formed by sequential depositions of Ge and BaF₂ $\lambda/4$ -thick films to form the DBRs. Figure 6(a) shows the cross-sectional scanning electron micrograph of an exemplar α_{LW} DBR, where the cross-section was prepared for imaging with the help of the FIB technique. It can be observed in Fig. 6(a) that the interface with the Si-substrate is well-defined and that the Ge and BaF₂ thin-films and interfaces are free from delamination and cracks. The degree of roughness that can be noted on the top surface is mainly associated with the cross-section preparation process, which used a highly FIB and is not a true representation of the as-fabricated surface roughness. Figures 6(b)–6(f) show material elemental maps over the cross-section obtained using EDS and further confirm the formation of well-defined thin-film interfaces. During this cross-sectional investigation, a minimal level of oxygen was found to be present (<1.7%) as reported in the compositional analysis shown in Fig. 6(g), which was evenly distributed throughout the films. Importantly, no increase in oxygen was observed neither at the thin-film interfaces nor within the thin films that could plausibly be associated with the cooling breaks during deposition. An overcoating gold layer was used to prevent charging effects during FIB/SEM investigations. These characteristics were observed to be common for both α_{MW} and α_{LW} DBRs. In the case of β -series DBRs cross-sectional analysis was not performed due to the expectation that the suspended membranes would collapse during the FIB cross-section preparation process. Nevertheless, we expect the β -series DBRs to show similar characteristics.

3.4 Membrane Flatness Profiles

Figure 7(a) shows an optical microscopic image of a released 500 $\mu\text{m} \times 500 \mu\text{m}$ β_{LW} - series DBR. The colour of the inner boundary of the unreleased area has been lightened for clarity. Figure 7(b) shows line-scans taken diagonally over the upper surface of all β_{LW} - series DBRs, as depicted in Fig. 7(a). The inset of Fig. 7(b) shows the same data on a magnified scale.

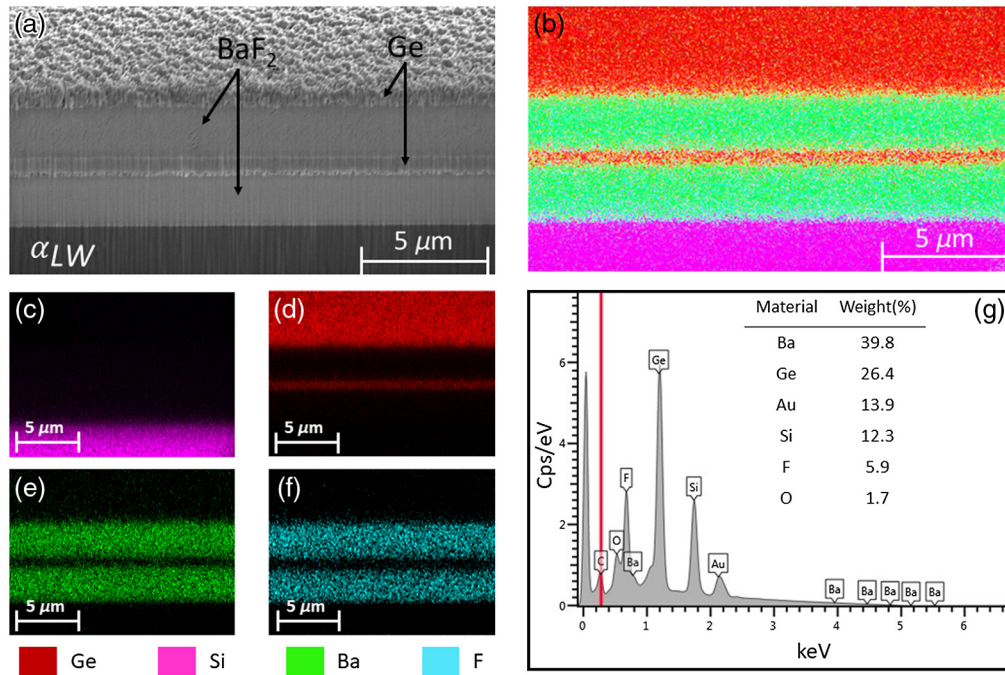


Fig. 6 FIB-SEM cross-section of α_{LW} , elemental mapping, and compositional analysis. The roughness in (a) on the top surface has been induced by the cross-section preparation process of the FIB method and is not representative of the actual as-fabricated thin-film surface roughness. Colour legend of the mapped elements is common to all elemental maps presented in (b)–(f). (g) Compositional analysis describing the weight (%) of each element present within the field of view. Images (b)–(f) are post-processed for better visualisation, and original images are provided in the appendix (see Fig. 13).

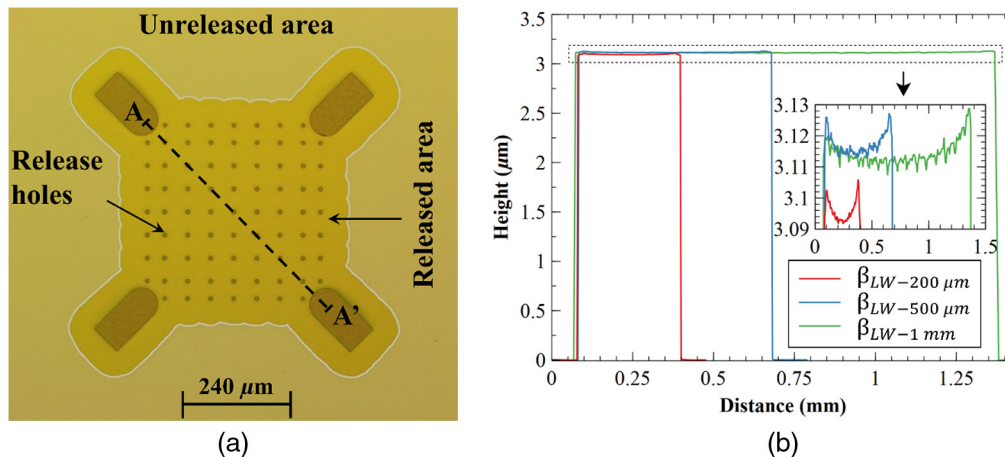


Fig. 7 (a) Micrograph of a dry released $500\ \mu\text{m} \times 500\ \mu\text{m}$ air-gap DBR. The edge profile has been drawn, and the colour of the unreleased area has been lightened to delineate the released area from the unreleased area. The dashed diagonal line AA' is indicative of the position in which the membrane flatness measurements were performed. (b) Line-scans taken diagonally over the optical surface of β_{LW} – series DBRs, indicating concave-upwards bowing of 10–20 nm was observed across the surface of fabricated LWIR DBRs. Profiles were measured for all device sizes using a Zygo Newview 6 K white light optical surface profiler. The rectangular area indicated by the dotted line in (b) is magnified vertically in the inset of (b).

A concave-upwards bowing of 10 to 20 nm was observed across the total released area in all three sizes of β_{LW} – series DBRs. The bowing within the optical area of the devices is limited to well below 10 nm, indicating very high surface flatness of the top Ge suspended layer taken over several hundred micrometers. Similarly, a high degree of flatness of the order of 5 to 10 nm was observed in the unpatterned α – series DBRs for similar line scan lengths. Since there are no suspended layers, it can be inferred that any bowing reported for the α – DBRs is mainly due to substrate deformation arising from film stress. The required level of flatness, in the range of <20 nm, was achieved for both α – and β – series DBRs and indicates that negligible performance degradation is expected since 20 nm of bowing is significantly below the required $\lambda/20$ optical condition at the center wavelength by more than two orders of magnitude.

3.5 DBR Reflectance Spectra

Figure 8 shows both simulated and measured reflectance of α – and β – series DBRs for single-point [Figs. 8(a) and 8(b)] and spatially distributed (multi-point) measurements [Fig. 8(c)].

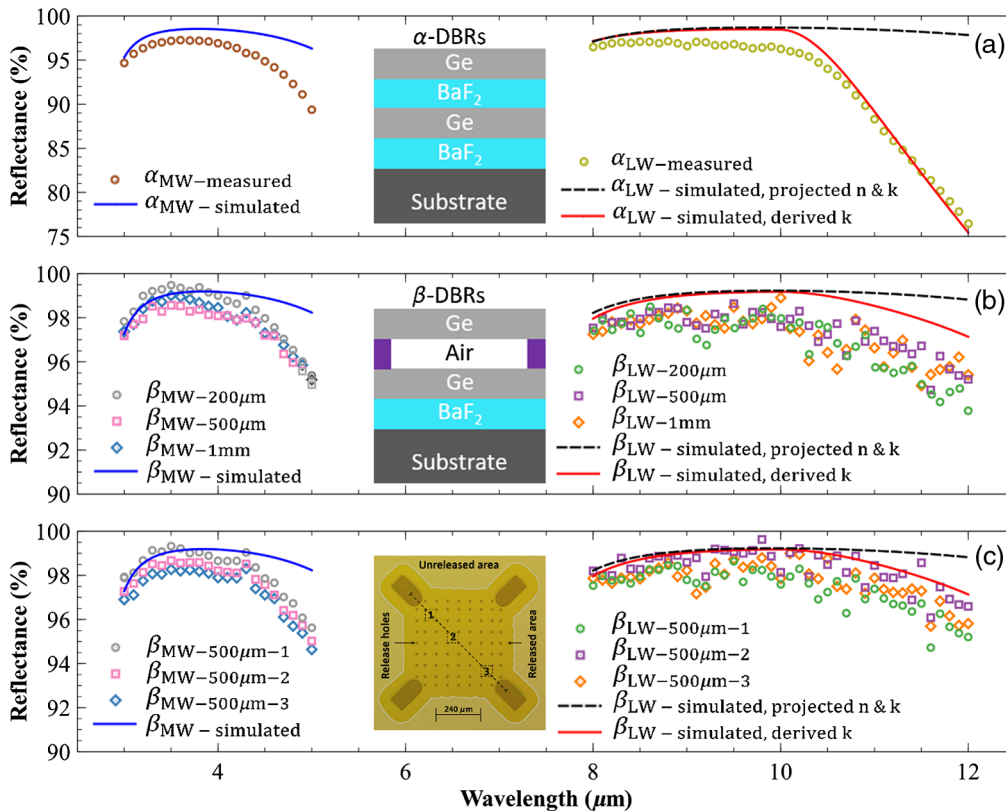


Fig. 8 Measured and simulated reflectance spectra for (a) α – and (b) β – series DBRs for single-point measurements at the DBR center, and (c) diagonally distributed (multi-point) reflectance spectra measurements over the suspended square area of a $500\ \mu\text{m} \times 500\ \mu\text{m}$ β – series DBR. The left and right sides of the figure show the data obtained for the MWIR and LWIR bands, respectively, using different α – and β – series DBR structures with thin-films of optical thicknesses appropriate for either MWIR or LWIR bands. The measurements in (b) have been performed at the center points of the $200\ \mu\text{m} \times 200\ \mu\text{m}$, $500\ \mu\text{m} \times 500\ \mu\text{m}$ and $1\ \text{mm} \times 1\ \text{mm}$ sized β – series DBRs. The simulated reflectance spectra in the MWIR band (solid blue lines) have been obtained using n - and k -values extracted from the measured transmission response of a $2.6\ \mu\text{m}$ thick BaF₂ layer, and for the LWIR region using n - and k -values that were projected linearly into the LWIR region from MWIR obtained data (dashed black lines), or using k -values (see Fig. 5 indicated as “ k -derived”) that were adjusted during the fitting iteration in order to achieve favourable agreement between measured and simulated reflectance spectra of α_{LW} (red solid lines).

The left and right sides of Fig. 8 show the data obtained for the MWIR and LWIR bands, respectively, originating from the characterization of different α - and β - series DBRs designed to operate specifically in the MWIR or LWIR band. The central insets provide the structural cross-sections of the measured devices [see Fig. 8(a) and 8(b)] and the top-view micrograph depicts the spatial position of measurements over the suspended β - series DBRs [see Fig. 8(c)]. A measurement spot size of approximately $35\ \mu\text{m} \times 35\ \mu\text{m}$ was adopted for the measurements. In the case of single-point measurements, only one measurement at the center of the DBR was performed. On the other hand, in the case of spatially distributed measurements, an array of measurements has been performed covering the entire optical area of the DBR, out of which data for three measurement points are presented for the $500\ \mu\text{m} \times 500\ \mu\text{m}$ sized β - series sample in Fig. 8(c). The left side of Fig. 8(a) shows that the peak reflectance value measured for α_{MW} (represented by brown open circles) was above 97% and was found to closely match the peak simulated reflectance value of 98.7% (represented by the blue solid line), which was obtained via simulations using experimentally extracted n and k values (see Fig. 5). However, although the simulated reflectance remains above 95% over the entire MWIR band, the measured reflectance values are reduced to nearly 90% for the long wavelength end of the MWIR region (approaching $5\ \mu\text{m}$). Nevertheless, even with 90% reflectance, these DBRs are viable candidates to produce narrow-band Fabry-Pérot (FP) filters in the MWIR region. Due to the solid structure of α - series DBRs, inter-layer bowing was not of concern, and there was little motivation to perform spatially distributed measurements.

The measured reflectance spectrum for α_{LW} [as shown by the yellow open circles on the right-hand side of Fig. 8(a)] was found to be characterised by a peak reflectance value of 97% and to remain above 96% for wavelengths between 8 and $10.2\ \mu\text{m}$. However, a notable drop in the measured reflectance was observed for longer wavelengths, which can be associated with increased absorption in the BaF₂ layer for wavelengths beyond $10.2\ \mu\text{m}$, resulting in a drop in the reflectance of α_{LW} to a value close to 75% at $12\ \mu\text{m}$. For wavelengths below $10.2\ \mu\text{m}$, good agreement was obtained between simulation [black dashed line in Fig. 8(a)] and experiment using the n - and k -values measured for wavelengths below $5.5\ \mu\text{m}$ and linearly extrapolating into the LWIR region (see Fig. 5). However, for simulations to match the measured data beyond $10\ \mu\text{m}$, the BaF₂ extinction coefficient needed to progressively increase with wavelength, reaching a value of close to 1 as wavelength approaches $12\ \mu\text{m}$ (refer to data in Fig. 5(b) indicated as “BaF₂ – derived”). The corresponding agreement between measurement and simulation can be observed in Fig. 8(a) by a comparison of data measured for α_{LW} with the OpenFilters simulation (red solid line) employing the derived values of k .

The observed decrease in the measured reflectance of α_{LW} for longer wavelengths could be related to the growth method of the BaF₂ thin-films, which may result in higher absorption in BaF₂ for wavelengths beyond $10.2\ \mu\text{m}$ in comparison to crystalline bulk BaF₂³² that can provide >70% transmission for wavelengths up to $11\ \mu\text{m}$. It is also important to note that the BaF₂ spacer layer experiences a longer heat treatment in comparison to the BaF₂ mirror layer sandwiched between the two Ge layers. This can also possibly lead to a change in thin-film morphology and impact the optical characteristics of the BaF₂ layer. Therefore, we anticipate the potential for process improvements that could lead to higher reflectance of α_{LW} beyond $10.2\ \mu\text{m}$ wavelengths; however, this is beyond the scope of the current study.

The left side of Fig. 8(b) shows three measured reflectance spectra for a single point measurement located at the center of each of the square β_{MW} DBRs of different areas and compares them to the simulated reflectance spectra predicted for this cross-sectional structure [depicted in the central inset of Fig. 8(b)]. An overall reflectance of above 94% was measured over the entire MWIR region for all three fabricated sizes. The reflectance measurements were in agreement with each other and were found to closely match the simulated reflectance spectrum where the overall reflectance value was predicted to remain above 97% within the entire MWIR region. Multiple single-point measurements were subsequently performed over the entire optical area to assess the reflectance spectra uniformity and repeatability for every point of observation. In the case of $500\ \mu\text{m} \times 500\ \mu\text{m}$ sized β - series samples, an array of 6×6 equally distributed measurements was used to cover the entire optical area. The left side of Fig. 8(c) shows the measured reflectance spectra obtained at three different locations along the diagonal for a $500\ \mu\text{m} \times 500\ \mu\text{m}$ sized β_{MW} DBR [as shown in the central inset of Fig. 8(c)]. All three

measured spectra compare favourably with the simulated reflectance data, which was obtained by OpenFilters software using the n - and k -values extracted from the transmission response of a 2.6 μm thick BaF₂ layer. The measured reflectance was found to remain above 94% over the entire MWIR region for all three measurements, which closely matches the simulated reflectance, which is predicted to remain above 97% for the entire MWIR band. The observed variation in the measured data represents the spread across all spatially distributed measurements spanning the entire optical area, which is confined to within <2%. This observation was found to be common for every spatially distributed point of observation over the entire optical area for all measured β_{MW} samples. As such, the observed uniformity in the spatially measured reflectance spectra can be correlated to the high degree of flatness of the suspended DBR layers.

Similar reflectance results were observed for β_{LW} single point and multiple point measurements. Single point measurements were performed at the center of each of the square DBRs of different areas. As presented on the right-hand side of Fig. 8(b), the measured reflectance value was found to remain above 94% over the entire LWIR region, with a peak reflectance value of 98% at wavelengths around 10 μm . These measured reflectance characteristics of β_{LW} compare favourably with the simulated reflectance values [represented by the red solid line on the right-hand side of Fig. 8(b)] obtained using the derived k -values for BaF₂ presented in Fig. 5(b), which are predicted to remain above 97% for the entire LWIR region. Notably, apart from a relatively insignificant difference of <2% near the long wavelength end (12 μm), a similar reflectance spectrum was obtained via simulation using n - and k -values of BaF₂ linearly extrapolated into the LWIR region (see Fig. 5), which is represented with a black dashed line on the right side of Fig. 8(b) and is characterised by a peak reflectance of above 99% along with an overall reflectance of more than 98% over the entire LWIR band. Since the reflectance values for all measured and simulated spectra for β_{LW} remain high, it is reasonable to attribute the drop in measured reflectance of α_{LW} as being solely due to the extra layer of BaF₂ centrally located within the α_{LW} DBR, which is not present in β_{LW} DBRs.

Similar to β_{MW} , spatially distributed (multi-point) measurements were performed over the entire optical area of β_{LW} . Exemplars of reflectance measurements for three different spots along the diagonal of the 500 $\mu\text{m} \times 500 \mu\text{m}$ sized β_{LW} are shown on the right-hand side of Fig. 8(c). For each measured β_{LW} spectrum the total reflectance was found to remain above 94% over the entire LWIR band, reaching a peak reflectance value of 99%. Furthermore, the spread across all spatially distributed measurements spanning the entire optical area is confined to within <2%. This was found to be common for all measured β_{LW} samples. Again, this high degree of uniformity in the spatially measured reflectance spectra can be correlated to the high degree of flatness of the suspended DBR layers.

Table 2 shows a comparison of the reflectance characteristics measured in this work with previously reported studies on surface micromachined DBRs in the MWIR and LWIR regions, along with the materials used to fabricate these DBRs. Prior literature reports peak reflectance values ranging from 90% to 94% in the MWIR region along with reflectance of $\geq 35\%$ over the entire MWIR band,^{25,56} whereas DBRs reported in this work have demonstrated superior peak reflectance of >97% and reflectance over the entire MWIR band surpassing 90%. In the case of LWIR DBRs, the results reported in this work have demonstrated superior or comparable peak reflectance and reflectance over the entire LWIR band of >97.5% and >94%, respectively, whereas peak reflectance and reflectance over the entire LWIR band in prior literature reports were >99% and >90%, respectively.⁵⁷

Summarizing the characteristics shown in Fig. 8, it can be stated that highly reflective β - series DBRs have been successfully fabricated for both MWIR and LWIR regions with good agreement between simulation and measurement, which renders them viable candidates for the fabrication of narrow FWHM MWIR and LWIR FP filters. In addition, α - series DBRs were also characterized to be highly reflective in the MWIR band making them suitable for the realization of narrow FWHM MWIR FP filters. However, a sharp drop in the measured reflectance spectra of α - series DBRs in the LWIR band observed for wavelengths longer than 10.2 μm limits their applicability in realizing narrow FWHM FP filters that cover the entire LWIR band. In spite of this, from a fabrication, reproducibility and uniformity point of view, α - series DBRs

Table 2 Comparison of results presented in this work with prior literature reports on surface micromachined DBRs in the MWIR and LWIR bands.

Wavelength region	DBR Materials	OEWB ^a (%)	PR ^a (%)	Ref.
MWIR (3 to 5 μm)	SiO _x /Si/Air/Si	>85 (3.75 to 6 μm)	94	25
	ZnSe/BaF ₂ /ZnSe/BaF ₂ /ZnSe	≥ 50	90 (abrupt interface)	56
		≥ 35	93 (graded interface)	
	BaF ₂ /Ge/Air/Ge	>90	97.2	This work
	BaF ₂ /Ge/BaF ₂ /Ge	>94	99	
LWIR (8 to 12 μm)	air/poly-Si/air/poly-Si	>99	100	57
		>90	>99	
	BaF ₂ /Ge/Air/Ge	>96.5	97.5	This work
	BaF ₂ /Ge/BaF ₂ /Ge	>94	99	

^aOEWB – Over entire wavelength band, PR – Peak reflectance.

are preferable since they do not contain any suspended layers and, hence, they are not subject to interlayer variability due to air-gap variations caused by stress imbalance or due to actuation.

4 Fabry–Pérot Interferometer for Infrared Imaging and Sensing

Based on the reflectance spectra demonstrated by DBRs in the MWIR and LWIR bands, we evaluated the suitability of α - and β - DBRs toward the realization of FPIs for hyperspectral sensing and imaging applications. For LWIR FPIs, this suitability is only assessed up to a wavelength of 11 μm due to excessive absorption within the BaF₂ layer beyond this wavelength. The α - and β - DBRs were used in three different combinations in an FPI arrangement to achieve a narrow linewidth of less than 30 to 50 nm and 80 to 110 nm in the case of MWIR and LWIR spectral bands, respectively, required for hyperspectral sensing and imaging applications. This involved assessment of the optical performance of (1) a solid-material FPI ($\alpha\alpha$ - FPI) consisting of a solid-material freestanding top DBR (α) and a solid-material fixed bottom DBR (α) on an Si substrate, separated by an air-gap optical cavity [represented on the left-hand side of Fig. 9(a)]; (2) a hybrid FPI ($\alpha\beta$ - FPI) consisting of an air-gap freestanding top DBR (β) and a solid-material fixed bottom DBR (α) on an Si substrate, separated by an air-gap optical cavity [see left-hand side of Fig. 9(b)]; (3) an air-gap FPI ($\beta\beta$ - FPI) consisting of an air-gap freestanding top DBR (β) and an air-gap fixed bottom DBR (β) on an Si substrate, separated by an air-gap optical cavity [see left-hand side of Fig. 9(c)]. The simulated optical performance of FPI structures consisting of these three combinations of α - and β - DBRs is shown on the right-hand side of Fig. 9. The transmission response plotted logarithmically in dB units is shown in Fig. 10 to present the expected out-of-band rejection performance. It is important to note that these simulation results are valid for imperfection-free FPIs, where fabrication induced variations are not considered, such as surface roughness and parallelism between the top and bottom DBRs. The $\lambda/4$ -thicknesses of the thin-films are presented in Table 1. In order to investigate the suitability of $\alpha\alpha$ -, $\alpha\beta$ - and $\beta\beta$ - FPIs, the optical transmission response of the FPIs was modeled for various optical cavity gaps in the MWIR and LWIR bands. In our modeling, a $\lambda/4$ -thick BaF₂ layer is present on both sides of a double-side polished <100> oriented 300 μm thick Si substrate. The BaF₂ layer on the front side serves as a spacer layer between the bottom DBR and the silicon substrate, and on the backside serves as an anti-reflection coating to suppress the effect of multiple reflections.

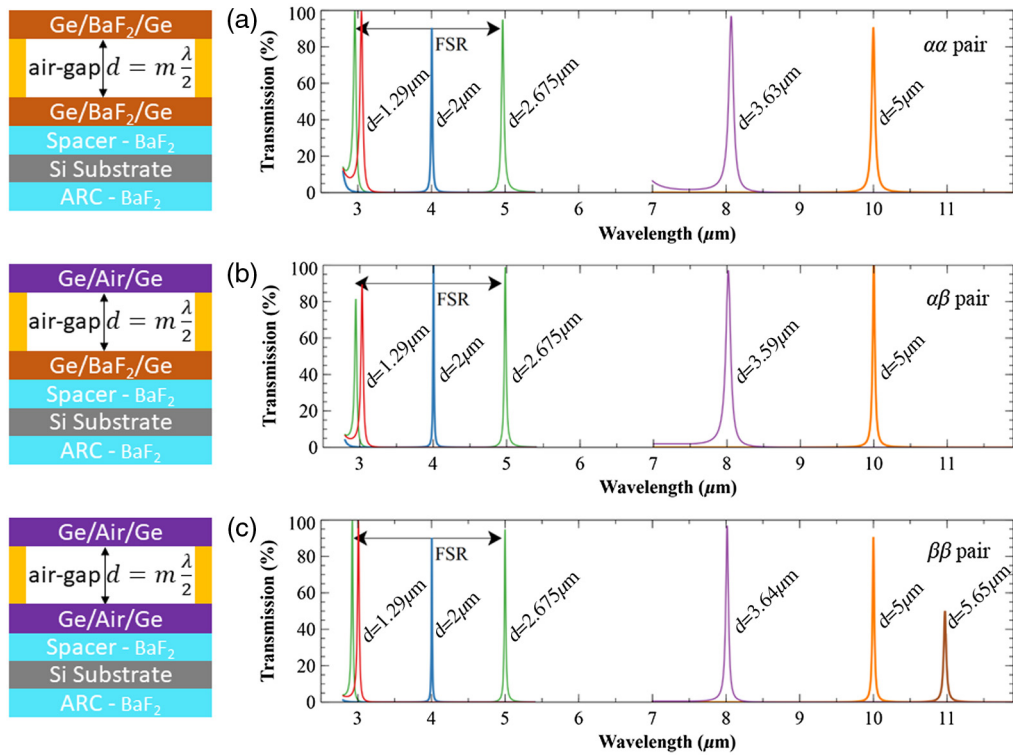


Fig. 9 Modeled optical transmission of two separate FPIs designed to operate in either the MWIR or LWIR spectral band by incorporating α - and β - series DBRs with different optical cavity lengths specific to the MWIR or LWIR spectral bands. Three combinations of DBRs (a) $\alpha\alpha$ - pairs, (b) $\alpha\beta$ - pairs and (c) $\beta\beta$ - pairs were investigated for spectral characteristics of FPIs. The corresponding cross-sectional geometries are presented schematically on the left-hand side and were designed for a center wavelength of 4 μm and 10 μm for MWIR and LWIR spectral bands, respectively. The air-gap optical cavity distance, d , separating the DBR pairs that determine the transmission wavelengths are indicated next to the peaks on the right-hand side. Exemplar FSR for the MWIR band is indicated for $d = 2.675 \mu\text{m}$ for all three DBR combinations as the wavelength separation between the first- and second-order FPI transmission peaks. In the case of LWIR, due to high optical absorption in the BaF₂ mirror layer beyond 10.2 μm , the extent of the LWIR FSR is not shown.

Figures 9 and 10 show exemplar transmission peaks, linewidths, and out-of-band rejection ratio of $\alpha\alpha$, $\alpha\beta$, and $\beta\beta$ based FPIs in the MWIR and LWIR regions for the designed center wavelengths as well as for the shorter and longer bounds of each wavelength band and are summarized in Fig. 11 for the full spectral band. For the longer wavelength bound where the first order transmission peak is located near a wavelength of 5 and 12 μm for MWIR and LWIR bands, respectively, the second-order transmission peak is located near the shorter wavelength end, which is also shown in Figs. 9 and 10 to indicate the extent of the free spectral range (FSR). Figures 11(a) and 11(b) presents a summary of the predicted peak transmission values and linewidth values, respectively, for the FPI transmission peaks over the full MWIR and LWIR spectral bands.

For the case of MWIR FPIs, a peak transmission above 90% for $\alpha\alpha$ - and $\beta\beta$ - FPIs and above 87% for $\alpha\beta$ - FPIs can be achieved over the entire MWIR band, as depicted for exemplar transmission peaks in Fig. 9 and summarized in Fig. 11(a) for the full spectral band. The transmission peaks for these FPIs are predicted to have a linewidth at the design center wavelength of 4 μm equal to 20 nm, 14 nm, and 11 nm for $\alpha\alpha$ -, $\alpha\beta$ - and $\beta\beta$ - FPIs, respectively, as shown in Fig. 9 and summarized in Fig. 11(b). The linewidth of FPIs was found to broaden by almost a factor of 3 in comparison to the linewidth at the center wavelength for wavelengths near the shorter and longer wavelength bounds of the MWIR band. Linewidth values of 51 and 40 nm, 39 and 28 nm, and 27 and 21 nm are predicted for the shorter and longer wavelength bounds of the MWIR band

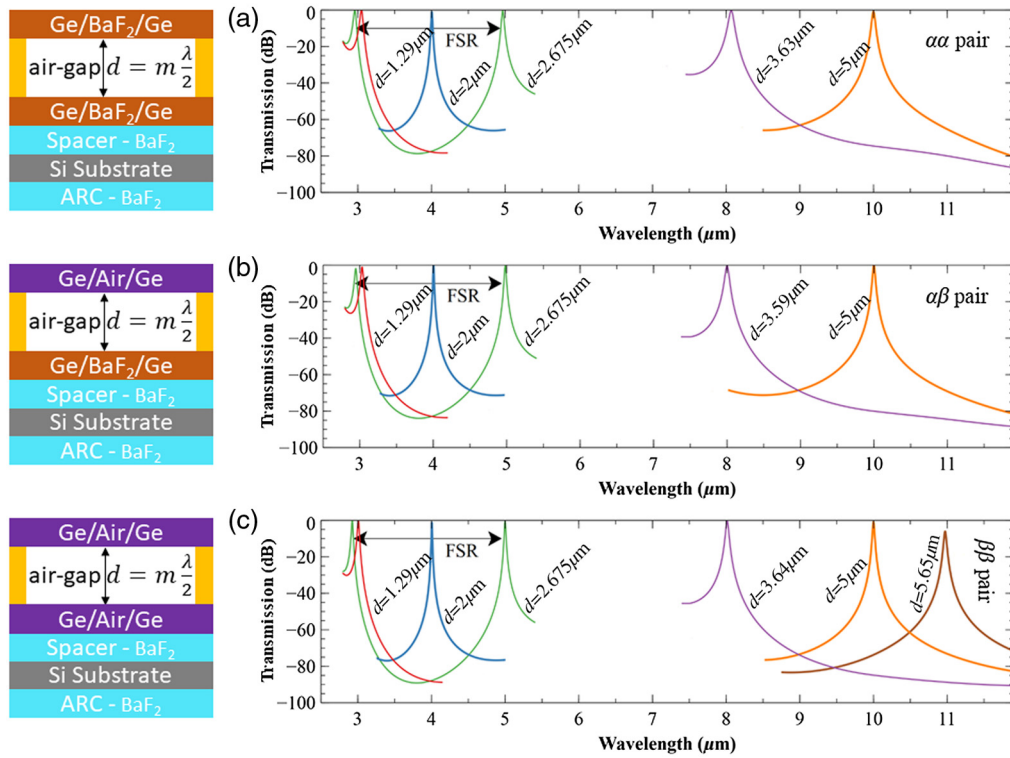


Fig. 10 Modeled optical transmission of FPIs plotted logarithmically in dB to more clearly illustrate the extinction coefficient of the FPIs.

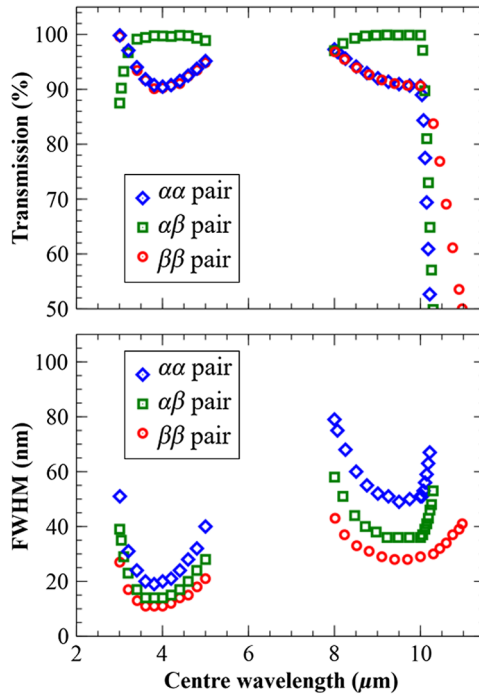


Fig. 11 The modeled (a) optical peak transmission and (b) FWHM values for FPIs designed for either the MWIR or LWIR spectral bands formed by $\alpha\alpha$, $\alpha\beta$, and $\beta\beta$ – pairs of DBRs.

for $\alpha\alpha$ -, $\alpha\beta$ - and $\beta\beta$ - FPIs, respectively. The simulation shows that an FSR of $> 2 \mu\text{m}$ can be achieved for $\alpha\alpha$ -, $\alpha\beta$ - and $\beta\beta$ - FPIs, as shown in Fig. 9. Furthermore, as shown in Fig. 10, the out-of-band rejection characteristics for the design center wavelength of $4 \mu\text{m}$ are predicted to be >65 , >70 , and >75 dB for $\alpha\alpha$ -, $\alpha\beta$ -, and $\beta\beta$ - FPIs, respectively. This is expected to reduce to ~ 20 dB (45 dB), 25 dB (50 dB), and 30 dB (50 dB) for the shorter (longer) wavelength ends of the MWIR band for $\alpha\alpha$ -, $\alpha\beta$ - and $\beta\beta$ - FPIs, respectively.

Similarly, the simulations of $\alpha\alpha$ -, $\alpha\beta$ -, and $\beta\beta$ - FPIs for the LWIR region show a peak transmission above 90% for $\alpha\alpha$ - FPIs and above 97% for $\alpha\beta$ - and $\beta\beta$ - FPIs can be achieved for the shorter wavelengths (8 to $10 \mu\text{m}$) of the LWIR band. The peak transmission drops to 50% at wavelengths of $10.2 \mu\text{m}$, $10.3 \mu\text{m}$ and $11 \mu\text{m}$ for $\alpha\alpha$ -, $\alpha\beta$ - and $\beta\beta$ - FPIs, respectively, which restricts the utilization of FPIs over the entire LWIR band. The simulations show that these FPIs have linewidth values equal to the 51, 36, and 29 nm of the center design wavelength of $10 \mu\text{m}$ for $\alpha\alpha$ -, $\alpha\beta$ -, and $\beta\beta$ - FPIs, respectively. The linewidth of the FPIs broadens by up to 1.6 times the linewidth value at the center design wavelength for wavelengths near the short wavelength end of the LWIR band. For wavelengths longer than $10 \mu\text{m}$, the peak transmission drops abruptly due to optical absorption in the BaF₂ mirror layer, therefore the extent of the LWIR FSR is not shown. The simulation data presented in Fig. 10 shows that for the design center wavelength of $10 \mu\text{m}$, out-of-band rejection ratios of >65 , >70 , and >75 dB can be achieved for $\alpha\alpha$ -, $\alpha\beta$ -, and $\beta\beta$ - FPI designs, respectively. This is expected to reduce to approximately 35, 40, and 45 dB for the shorter end ($8 \mu\text{m}$) of the LWIR band for $\alpha\alpha$ -, $\alpha\beta$ -, and $\beta\beta$ - FPIs, respectively.

The simulated spectral characteristics of FPIs are summarized in Table 3 and, for comparison, a set of optical requirements of FPIs for hyperspectral sensing and imaging applications. Typically, to perform hyperspectral sensing and imaging, it is required to have the peak transmission above 50% and the spectral width below 1% of the design wavelength. In the case of MWIR FPIs, a linewidth of much lower than 1% of the targeted wavelength can be easily achieved for wavelengths between 3.2 and $5 \mu\text{m}$ using $\alpha\alpha$ - and $\alpha\beta$ - pair FPIs and over the entire MWIR spectrum for $\beta\beta$ - FPIs, as shown in Fig. 11(b). The linewidth broadens up to 1.7% (51 nm) and 1.3% (39 nm) of the design wavelength for $\alpha\alpha$ - and $\alpha\beta$ - FPIs, respectively, while still covering the entire MWIR band. This linewidth over the entire MWIR spectrum is very useful for hyperspectral sensing and imaging applications. For LWIR FPIs, the peak transmission starts to drop abruptly after $10 \mu\text{m}$, which limits their operating range in the LWIR region. The simulations show that for $\alpha\alpha$ -, $\alpha\beta$ -, and $\beta\beta$ - FPIs, the peak transmission drops to a level below 50% for wavelengths longer than 10.2 , 10.3 , and $11 \mu\text{m}$, respectively [as depicted in Fig. 11(a)], and is associated with absorption phenomena observed in the

Table 3 Comparison between the required and simulated spectral characteristics for FPIs in the MWIR and LWIR spectral bands for hyperspectral imaging applications.

FPIs	Structural geometry (DBR combination)	Peak transmission		Spectral width	
		Required	Simulated	Required	Simulated
MWIR (3 to $5 \mu\text{m}$)	Solid-material FPI ($\alpha\alpha$ - pair)	$>50\%$	$>90\%$	30 to 50 nm	19 to 51 nm
	Hybrid FPI ($\alpha\beta$ - pair)		$>87\%$		14 to 39 nm
	Air-gap FPI ($\beta\beta$ - pair)		$>90\%$		11 to 27 nm
LWIR (8 to $11 \mu\text{m}$)	Solid-material FPI ($\alpha\alpha$ - pair)	$>50\%$	$>52\%$ (8 to $10.2 \mu\text{m}$)	80 to 110 nm	49 to 79 nm (8 to $10.2 \mu\text{m}$)
	Hybrid FPI ($\alpha\beta$ - pair)		$\geq 50\%$ (8 to $10.3 \mu\text{m}$)		36 to 58 nm (8 to $10.3 \mu\text{m}$)
	Air-gap FPI ($\beta\beta$ - pair)		$>50\%$ (8 to $11 \mu\text{m}$)		28 to 43 nm (8 to $11 \mu\text{m}$)

BaF₂ mirror layer for longer wavelengths. The $\alpha\alpha$ -, $\alpha\beta$ -, and $\beta\beta$ - FPIs demonstrated a narrow linewidth of less than 1% of the design wavelength for wavelengths 8 to 10.2 μm , 8 to 10.3 μm , and 8 to 11 μm , respectively, in the LWIR spectral band along with peak transmission above 50%.

The FPI simulations based on the optical performance of the DBRs in the MWIR spectrum show that all three combinations of $\alpha\alpha$ -, $\alpha\beta$ -, and $\beta\beta$ - FPIs can satisfy the optical requirements needed for hyperspectral sensing and imaging applications across the MWIR band. For the LWIR case, the peak transmission drops abruptly for wavelengths above 10 μm due to absorption losses in the BaF₂ mirror layers, allowing these FPIs to be used only within the shorter wavelength half of the LWIR band (8 to 10 μm) along with the attractive peak transmission of above 90%. This range can be extended up to 10.2, 10.3, and 11 μm with a peak transmission of above 50% for $\alpha\alpha$ -, $\alpha\beta$ - and $\beta\beta$ - FPIs along with linewidth of <1%, as shown in Fig. 11. Hence, we can conclude that $\alpha\alpha$ -, $\alpha\beta$ - and $\beta\beta$ - FPIs can be used for wavelengths in the 8 to 11 μm range based on their structural geometry while maintaining a spectral transmission above 50% and a linewidth below 1%. Additionally, simulation results presented in Figs. 9–11 show that the $\beta\beta$ - FPIs are superior and have more potential to produce narrowband FPIs. However, it is very difficult to fabricate these FPIs due to their complex fabrication process with multiple air-gaps. On the other hand, $\alpha\alpha$ - FPIs based on solid-material DBRs are the most practical approach to realize narrowband FPIs from the fabrication point of view since α - series DBRs are not subject to interlayer variability due to air-gap variations caused by stress imbalance or during actuation in a tunable filter FPI configuration.

5 Summary and Conclusions

The fabrication and optical characterization of Ge and BaF₂ based solid-material and air-gap (α - and β - series) DBRs have been presented in this paper. DBRs with high reflectivity were designed and demonstrated for operation in either the MWIR or LWIR wavelength ranges. In the case of α - series DBRs, a drop in reflectance of the DBRs is noticed toward the long wavelength end of the wavelength range in both the MWIR (3 to 5 μm) and LWIR (8 to 12 μm) spectral bands. The MWIR DBRs demonstrated a moderate drop in the measured reflectance, to 90%, in comparison to the simulated reflectance of 95%. However, for LWIR DBRs, the reflectance drops sharply after 10 μm and reaches 76%, at a wavelength of 12 μm , which limits their applicability in the realization of narrow FWHM Fabry-Pérot filters over the entire LWIR band. On the other hand, β - series DBRs were demonstrated with optical dimensions of 200 $\mu\text{m} \times 200 \mu\text{m}$, 500 $\mu\text{m} \times 500 \mu\text{m}$ and 1 mm \times 1 mm, and exhibited flatness of the order of 10 to 20 nm over the entire optical area. Single point spectral measurements at the center of devices show good agreement with simulated optical models for both MWIR and LWIR DBRs. The fabricated β - series DBRs have reflectance over 94%, in comparison to the simulated reflectance above 97%. Multiple single point measurements were also performed to evaluate the reflectance spectra uniformity and repeatability for every point of observation over the entire optical area, especially in the case of β - series DBRs and to confirm a high degree of reflectance uniformity over the entire optical area.

The DBR experimental results extend the current MEMS approach toward the fabrication of FPIs for narrow-band hyperspectral sensing and imaging applications. To this end, optical transmission of three different types of solid, hybrid, and air-gap ($\alpha\alpha$, $\alpha\beta$, and $\beta\beta$, respectively) FPIs was examined based on three-layer α - and β - series DBRs in the MWIR and LWIR spectral bands. Optical modeling indicates that in the case of the MWIR region, the $\alpha\alpha$ -, $\alpha\beta$ -, and $\beta\beta$ - FPIs cover 90% of the MWIR spectral band with peak transmission above 90% and spectral width <1% of the targeted wavelength. However, for the LWIR spectral band, the $\alpha\alpha$ -, $\alpha\beta$ -, and $\beta\beta$ - FPIs provide an operating range of 8 to 10.2 μm , 8 to 10.3 μm and 8 to 11 μm , respectively, while maintaining the peak transmission above 50%, with a narrow spectral linewidth <1% of the targeted wavelength, which exceeds the optical requirements for hyperspectral imaging applications.

6 Appendix

Figure 12 provides the actual thicknesses of thermally deposited $\lambda/4$ -thick optical thin-films, measured using Dektak 150 surface profiler. Figures 12(a) and 12(b) represent the solid-material and air-gap (α - and β - series) DBRs designed in MWIR and LWIR spectral bands, respectively. Figure 13 provides original images of structural characterization of α_{LW} DBR. Figure 13(a) shows the cross-sectional scanning electron micrograph. Figures 13(b)–13(f) shows material elemental maps over the cross-section, and the compositional analysis is shown in Fig. 13(g).

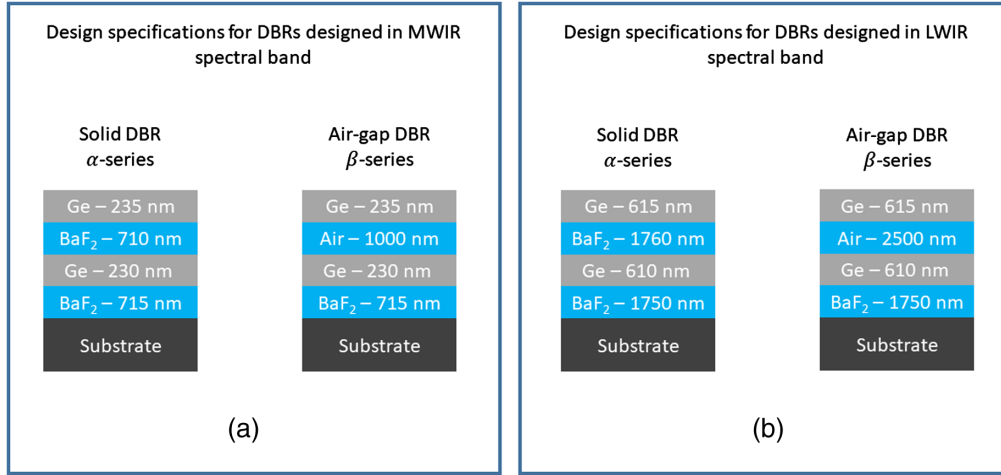


Fig. 12 Design specifications of solid-material and air-gap (α - and β - series) DBRs designed in (a) MWIR and (b) LWIR spectral bands.

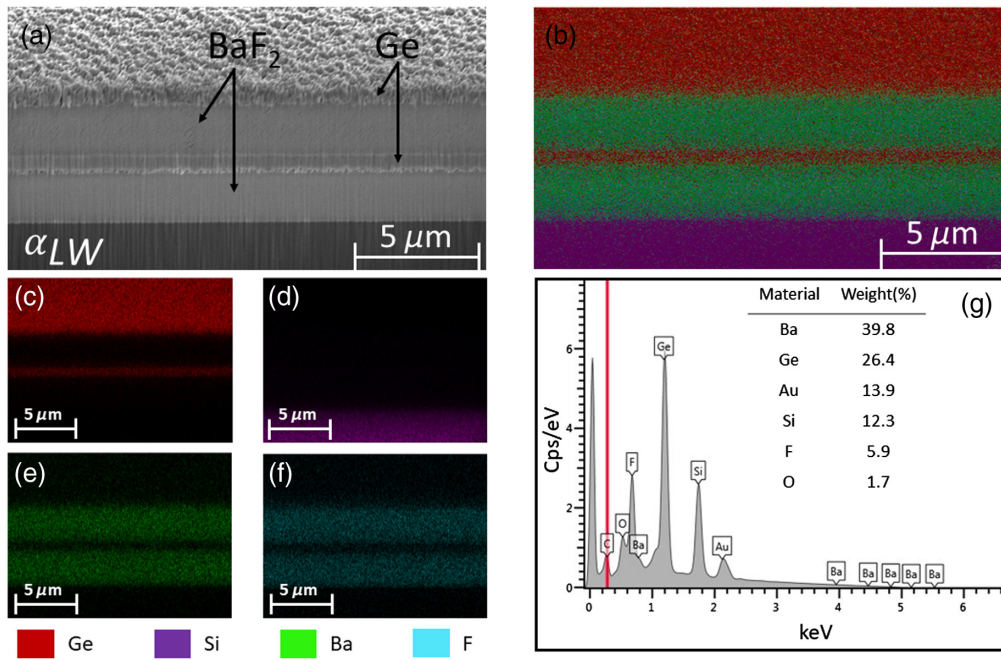


Fig. 13 (a) FIB-SEM cross-section of α_{LW} , (b)–(f) elemental mapping, and (g) compositional analysis. Colour legend of the mapped elements is common to all elemental maps presented in (b)–(f).

Acknowledgments

This work used the facilities of the Western Australian node of the NCRIS-enabled Australian National Fabrication Facility (ANFF), a company established under the National Collaborative Research Infrastructure Strategy to provide nano- and micro-fabrication facilities for Australia's researchers, and support from the Western Australian Government's Department of Jobs, Tourism, Science and Innovation. This research was supported financially by Australian Research Council Discovery Project grants. The authors also thankfully acknowledge the facilities, and the scientific and technical assistance of the Center for Microscopy, Characterization & Analysis (CMCA); and The University of Western Australia for the Scholarship for International Research Fees; and The Microelectronics Research Group (MRG) for an Ad Hoc Postgraduate Scholarship. There is no conflict of interest.

References

1. M. Ebermann et al., "Widely tunable Fabry–Perot filter based MWIR and LWIR microspectrometers," *Proc. SPIE* **8374**, 83740X (2012).
2. M. Ebermann et al., "Tiny mid- and long-wave infrared spectrometer module with a MEMS dual-band Fabry–Pérot filter," in *IRS2 Proc. - SENSOR+TEST Conf.*, pp. 94–99 (2011).
3. M. Ebermann et al., "Tunable MEMS Fabry–Pérot filters for infrared microspectrometers: a review," *Proc. SPIE* **9760**, 97600H (2016).
4. M. Ebermann et al., "Design, operation and performance of a Fabry–Perot-based MWIR microspectrometer," in *IRS2 Proc. - SENSOR+TEST Conf.*, Vol. 1, pp. 233–238 (2009).
5. D. Wang et al., "MWIR thermal imaging spectrometer based on the acousto-optic tunable filter," *Appl. Opt.* **56**(25), 7269–7276 (2017).
6. F. Kühnemann, "Mid-infrared spectrometer," 2019, www.ipm.fraunhofer.de/en (accessed 11 Aug 2021).
7. R. G. Vaughan et al., "Surface mineral mapping at Steamboat Springs, Nevada, USA, with multi-wavelength thermal infrared images," *Remote Sens. Environ.* **99**(1–2), 140–158 (2005).
8. B. J. Craig et al., "Mid- to long-wave infrared computational spectroscopy using a sub-wavelength coaxial aperture array," *Sci. Rep.* **9**(1), 13537 (2019).
9. V. R. Shrestha et al., "Mid- to long-wave infrared computational spectroscopy with a graphene metasurface modulator," *Sci. Rep.* **10**(1), 5377 (2020).
10. S. Wolf et al., "High-speed MWIR upconversion spectroscopy," in *AMA Conf. 2017 – SENSOR 2017 and IRS2 2017*, pp. 766–768 (2020).
11. S. Wolf et al., "MWIR upconversion detection for infrared gas spectroscopy," in *3D Image Acquisition and Display: Technology, Perception and Applications*, pp. JW1F-6, Optical Society of America (2016).
12. H. Mao et al., "Large-area MEMS tunable Fabry–Perot filters for multi/hyperspectral infrared imaging," *IEEE J. Sel. Top. Quantum Electron.* **23**(2), 2700208 (2017).
13. J. Silva et al., "MEMS-based Low SWaP solutions for multi/hyperspectral infrared sensing and imaging," in *RAPID 2018-2018 IEEE Res. and Appl. of Photonics in Defense Conf.*, pp. 189–192 (2018).
14. K. Uto et al., "Development of a low-cost hyperspectral whiskbroom imager using an optical fiber bundle, a swing mirror, and compact spectrometers," *IEEE J. Sel. Top. Appl. Earth Obs. Remote Sens.* **9**(9), 3909–3925 (2016).
15. K. Uto et al., "Development of lightweight hyperspectral imaging system for UAV observation," in *Workshop on Hyperspectral Image and Signal Process., Evol. in Remote Sens.* (2014).
16. M. Martyniuk et al., "Optical microelectromechanical systems technologies for spectrally adaptive sensing and imaging," *Adv. Funct. Mater.* **2103153**, 1–8 (2021).
17. R. Vandersmissen and T. Zimmermann, "MWIR for remote sniffing and locating of gases," 2014, https://www.photonics.com/Articles/MWIR_for_Remote_Sniffing_and_Locating_of_Gases/a56861 (accessed 11 Aug. 2021).
18. M. Govender, K. Chetty, and H. Bulcock, "A review of hyperspectral remote sensing and its application in vegetation and water resource studies," *Water SA* **33**(2), 145–151 (2007).

19. F. Vagni, "Survey of hyperspectral and multispectral imaging technologies," 2007, <https://ntrl.ntis.gov/NTRL/dashboard/searchResults/titleDetail/ADA473675.xhtml> (accessed 11 Aug. 2021).
20. A. Rissanen, R. Mannila, and J. Antila, "Bragg reflectors for large optical aperture MEMS Fabry–Perot interferometers," *Proc. SPIE* **8373**, 83732R (2012).
21. J. S. Milne et al., "Widely tunable MEMS-based Fabry–Perot Filter," *J. Microelectromech. Syst.* **18**(4), 905–913 (2009).
22. S. S. Wang and R. Magnusson, "Theory and applications of guided-mode resonance filters," *Appl. Opt.* **32**(14), 2606 (1993).
23. S. Tibuleac and R. Magnusson, "Reflection and transmission guided-mode resonance filters," *J. Opt. Soc. Am. A* **14**(7), 1617 (1997).
24. Y. H. Ko et al., "Micro-electromechanical-system-tuned resonant filters spanning the 8 to 12 μm band," *Opt. Lett.* **46**(6), 1329 (2021).
25. D. K. Tripathi et al., "Large-area MEMS-based distributed Bragg reflectors for short-wave and mid-wave infrared hyperspectral imaging applications," *J. Microelectromech. Syst.* **24**(6), 2136–2144 (2015).
26. J. R. Silva et al., "Large area silicon-air-silicon DBRs for infrared filter applications," *J. Lightwave Technol.* **37**(3), 769–779 (2019).
27. H. Mao et al., "Ge/ZnS-based micromachined Fabry–Perot filters for optical MEMS in the longwave infrared," *J. Microelectromech. Syst.* **24**(6), 2109–2116 (2015).
28. H. A. Macleod, *Thin-Film Optical Filters*, 2nd ed., Adam Hilger Ltd., Bristol (1986).
29. T. Amotchkina et al., "Characterization of e-beam evaporated Ge, YbF₃, ZnS, and LaF₃ thin films for laser-oriented coatings," *Appl. Opt.* **59**(5), A40 (2020).
30. H. W. Icenogle, B. C. Platt, and W. L. Wolfe, "Refractive indexes and temperature coefficients of germanium and silicon," *Appl. Opt.* **15**(10), 2348–2351 (1976).
31. W. Kaiser et al., "Infrared properties of CaF₂, SrF₂, and BaF₂," *Phys. Rev.* **127**(6), 1950–1954 (1962).
32. M. R. Querry, *Optical Constants of Minerals and Other Materials from the Millimeter to the Ultraviolet*, Aberdeen Proving Ground, Maryland (1987).
33. H. Mao et al., "MEMS-based tunable Fabry–Perot filters for adaptive multispectral thermal imaging," *J. Microelectromech. Syst.* **25**(1), 227–235 (2016).
34. H. Mao et al., "Towards longwave infrared tuneable filters for multispectral thermal imaging applications," 2014, www.ndt.net/?id=17694 (accessed 15 April 2020).
35. A. J. Keating et al., "Design and characterization of Fabry–Perot MEMS-based short-wave infrared microspectrometers," *J. Electron. Mater.* **37**(12), 1811–1820 (2008).
36. M. Meinig et al., "Dual-band MEMS Fabry–Perot filter with two movable reflectors for mid- and long-wave infrared microspectrometers," in *16th Int. Solid-State Sens., Actuators and Microsyst. Conf., TRANSDUCERS'11*, pp. 2538–2541 (2011).
37. L. Kirkland et al., "First use of an airborne thermal infrared hyperspectral scanner for compositional mapping," *Remote Sens. Environ.* **80**(3), 447–459 (2002).
38. D. Gu et al., "Autonomous atmospheric compensation (AAC) of high resolution hyperspectral thermal infrared remote-sensing imagery," *IEEE Trans. Geosci. Remote Sens.* **38**(6), 2557–2570 (2000).
39. B. Lu et al., "Recent advances of hyperspectral imaging technology and applications in agriculture," *Remote Sens.* **12**(16), 2659 (2020).
40. A. Behranvand et al., "Design and fabrication of PbTe/BaF₂ hydrophobic high-efficiency broad-band antireflection coating on Ge substrate in long-wave infrared region," *Infrared Phys. Technol.* **92**, 163–165 (2018).
41. T. D. Rahmlow et al., "Dual band antireflection coatings for the infrared," *Proc. SPIE* **6940**, 69400T (2008).
42. "BaF₂ barium fluoride scintillation material," www.crystals.saint-gobain.com (accessed 01 June 2021).
43. M. Ghaderi et al., "Optical characterization of MEMS-based multiple air-dielectric blue-spectrum distributed Bragg reflectors," *Proc. SPIE* **9517**, 95171M (2015).
44. M. Ghaderi, G. De Graaf, and R. F. Wolffenbuttel, "Fabrication of ultrathin large-area dielectric membrane stacks for use as interference filters," *Procedia Eng.* **168**, 1342–1345 (2016).

45. H. Urey, D. W. Wine, and T. D. Osborn, "Optical performance requirements for MEMS-scanner-based microdisplays," *Proc. SPIE* **4178**, 176–185 (2000).
46. C. L. Tien, Y. R. Lyu, and S. S. Jyu, "Surface flatness of optical thin films evaluated by gray level co-occurrence matrix and entropy," *Appl. Surf. Sci.* **254**(15), 4762–4767 (2008).
47. "Quartz crystal - inficon," <https://www.inficon.com/en/products/quartz-crystal> (accessed 28 July 2021).
48. "Front load single and dual sensors," INFICON, 2014, www.inficon.com (accessed 08 April 2020).
49. G. G. Stoney, "The tension of metallic films deposited by electrolysis," *Proc. R. Soc.* **82**, 172–175 (1909).
50. X. Feng, Y. Huang, and A. J. Rosakis, "On the Stoney formula for a thin film/substrate system with nonuniform substrate thickness," *J. Appl. Mech.* **74**(6), 1276 (2007).
51. S. Larouche and L. Martinu, "OpenFilters: open-source software for the design, optimization, and synthesis of optical filters," *Appl. Opt.* **47**(13), C219 (2008).
52. H. A. Macleod, *Thin-Film Optical Filters*, 4th ed., pp. 1–782, CRC Press, Taylor & Francis Group, Boca Raton, London, New York (2010).
53. E. D. Palik, *Handbook of Optical Constants of Solids I-III*, Academic Press, San Diego (1998).
54. S. Bosch, J. Ferré-Borrull, and J. Sancho-Parramon, "A general-purpose software for optical characterization of thin films: Specific features for microelectronic applications," *Solid. State. Electron.* **45**(5), 703–709 (2001).
55. Optical constants of Si (Silicon), "Refractive index of Si (Silicon) - Shkondin," <https://refractiveindex.info/?shelf=main&book=Si&page=Shkondin> (accessed 25 Aug. 2021).
56. D. Admassu et al., "Effect of interface grading on the optical performance of distributed Bragg reflector multilayers in Fabry–Pérot optical filters," *Microsyst. Technol.* **27**(7), 2785–2790 (2021).
57. M. Tuohiniemi and M. Blomberg, "Surface-micromachined silicon air-gap Bragg reflector for thermal infrared," *J. Micromech. Microeng.* **21**, 075014 (2011).

Gurpreet S. Gill received his BTech and MTech degrees in electronics and communication engineering from the Punjab Technical University and Sri Guru Granth Sahib World University, Punjab, India, in 2013 and 2015, respectively. He is currently pursuing his PhD with the Department of Electrical, Electronic and Computer Engineering, University of Western Australia (UWA), Perth, Australia. His current research activities involve thin-film materials and optical micro-electro-mechanical systems for multi-/hyper-spectral imaging and sensing applications.

Dhirendra K. Tripathi received his BTech degree in electronics engineering from Uttar Pradesh Technical University, Lucknow, India, in 2005, the MTech degree in VLSI systems from the National Institute of Technology, Tiruchirappalli, India, in 2008, and the PhD from UWA, Perth, Australia, in 2016. He is currently a postdoctoral researcher with the University of Western Australia. His research activities involve design and fabrication of optical MEMS devices and materials for the MEMS.

Adrian Keating received his BE and PhD degrees in electrical and electronic engineering from the University of Melbourne, Australia, in 1990 and 1995, respectively. In 2004, he joined the School of Electrical, Electronic and Computer Engineering, UWA, Perth, Australia, moving to the School of Mechanical Engineering in 2007 as an associate professor, and became a professor in 2010. His current research activities are in the field of optical microelectro-mechanical systems and porous silicon-based sensor technologies.

Gino Putrino received his BSc degree in computer science and the BE degree in electrical and electronic engineering from UWA, Perth, Western Australia, Australia, in 1999, and the PhD in 2014. His research interests involve the use of optical microelectro-mechanical systems (MEMS) and silicon photonics to create novel chemical and biological sensing devices.

Konkaduwa Kamala Mesthrige Buddhika Dilusha Silva received his honors degrees in physics and electronic engineering from UWA, Perth, Australia, and the PhD in optical imaging

technologies for biomedical applications in 2004. He has worked both in industry and academia, and is currently with the Microelectronics Research Group, UWA. His research interests have included optical MEMS sensors, optical spectroscopic sensors, and atmospheric optics.

Mariusz Martyniuk received his BSc (Hons.) degree from the University of Toronto, MASc from McMaster University, and the PhD from UWA in 2007. He worked in the industry sector as an electronics engineer before rejoining UWA, where he is currently with the Microelectronics Research Group and manages the Western Australian Node of the Australian National Fabrication Facility. His primary areas of interest encompass thin-film materials and thin-film mechanics, as well as their applications in micro-electromechanical systems and optoelectronic devices.

Lorenzo Faraone received his PhD from UWA, Perth, Western Australia, Australia, in 1979. He joined the School of Electrical, Electronic and Computer Engineering, UWA, in 1987, where he has been a professor since 1998, and the head of the department/school from 1999 to 2003. Since joining UWA, his research interests have been in the areas of compound semiconductor materials and devices, and microelectromechanical systems.